# The 2021 Mw 7.3 East Cape earthquake: Triggered Rupture in Complex Faulting Revealed by Multi-Array Back-projections

**Y.Xie[1], L. Meng[1] , T. Zhou[1], L. Xu[1], H. Bao[1], R. Chu[2]**

[1]Earth, Planetary and Space Sciences, University of California, Los Angeles, CA 90025, USA.

[2]State Key Laboratory of Geodesy and Earth's Dynamics, Innovation Academy for Precision Measurement Science and Technology, Chinese Academy of Sciences, Wuhan, China

Corresponding author: Lingsen Meng (meng@epss.ucla.edu)， Risheng Chu (chur@apm.ac.cn)

**Key Points:**

- We apply a multi-array 3D back-projection to image the rupture process of the 2021 Mw 7.3 East Cape earthquake
- Our results reveal a bilateral rupture predominantly propagating upward from 70 km and a triggered rupture at ~ 10 km.
- The deep rupture is in the mantle of the subducting Pacific plate, which is possibly related to a delaminating lower crust.

**Abstract**

On March 04, 2021 the Mw 7.3 East Cape, New Zealand earthquake occurred at the southern end of the Kermadec Trench. The USGS W-phase solution shows an unexpected focal mechanism compared to historical earthquakes. We combine earthquake back-projections of 4 arrays to image the kinematic process of the Mw 7.3 earthquake. Our results reveal a bilateral rupture predominantly propagating upward at a slow speed of 1 km/s and a triggered rupture at ~ 10 km, corresponding to the deep reverse faulting event at 70 km and a triggered shallow normal faulting event (~20 km) resolved by previous subevent and finite fault inversions. The epicenter and a group of aftershocks are deeper than the bottom of the slab according to a regional tomography model. Such deep failure is possibly enabled by a delaminating lower crust of the Hikurangi plateau.

**Plain Language Summary**

On March 04, 2021 the Mw 7.3 East Cape, New Zealand earthquake occurred at the southern end of the Kermadec Trench. Previous studies indicate that this earthquake ruptured multiple faults of different orientations. We apply a method using the recordings of 4 arrays of closely spaced sensors receiving earthquake signals to calculate the details of the earthquake source. Our results reveal that the rupture first propagates upward from 70 km at a slow speed of 1 km/s then then a shallow rupture at ~ 10 km is imaged. This result is consistent with the two subevents imaged by previous studies (Okuwaki et al., 2021). The earthquake source and a group of aftershocks are in the mantle of the subducting Pacific plate, which is unusual because earthquake is prohibited due to high temperature and pressure. Such deep failure is possibly enabled by the sinking of part of the crust into the mantle.

## 1 Introduction

On March 04, 2021, a Mw 7.3 earthquake occurred approximately 182 km to the northeast of the city of Gisborne, at the southern end of the Kermadec Trench, where the Hikurangi Plateau underthrusts beneath the Australian plate. The Mw 7.3 event is followed by two larger Mw 7.4 and Mw 8.1 quakes ~ 4 hours later ~ 800 km to the north (Okuwaki et al., 2021). The thickness of Hikurangi Plateau is approximately 12 - 15 km (the average thickness of Pacific oceanic crust is 8 km), close to the critical thickness (17 km) where buoyancy switches from driving to resisting subduction (Collot and Davy, 1998). Due to the thickening of the oceanic plate and the increasing obliquity from north to south, the convergence rate decreases from 6.3 cm/yr near 30°S to 4.9 cm/yr at 37°S (de Mets et al., 1990). The subduction stops around 44° S, where the Chatham Rise indicates the transition from oceanic to continental crust of the Pacific plate. The obliquity in the Hikurangi trench causes a slip-partitioning motion with the trench-parallel motion accommodated by strike-slip faulting and the rotation of the eastern North Island arc (Wallace and Beavan, 2004; Wallace and Beavan, 2010).

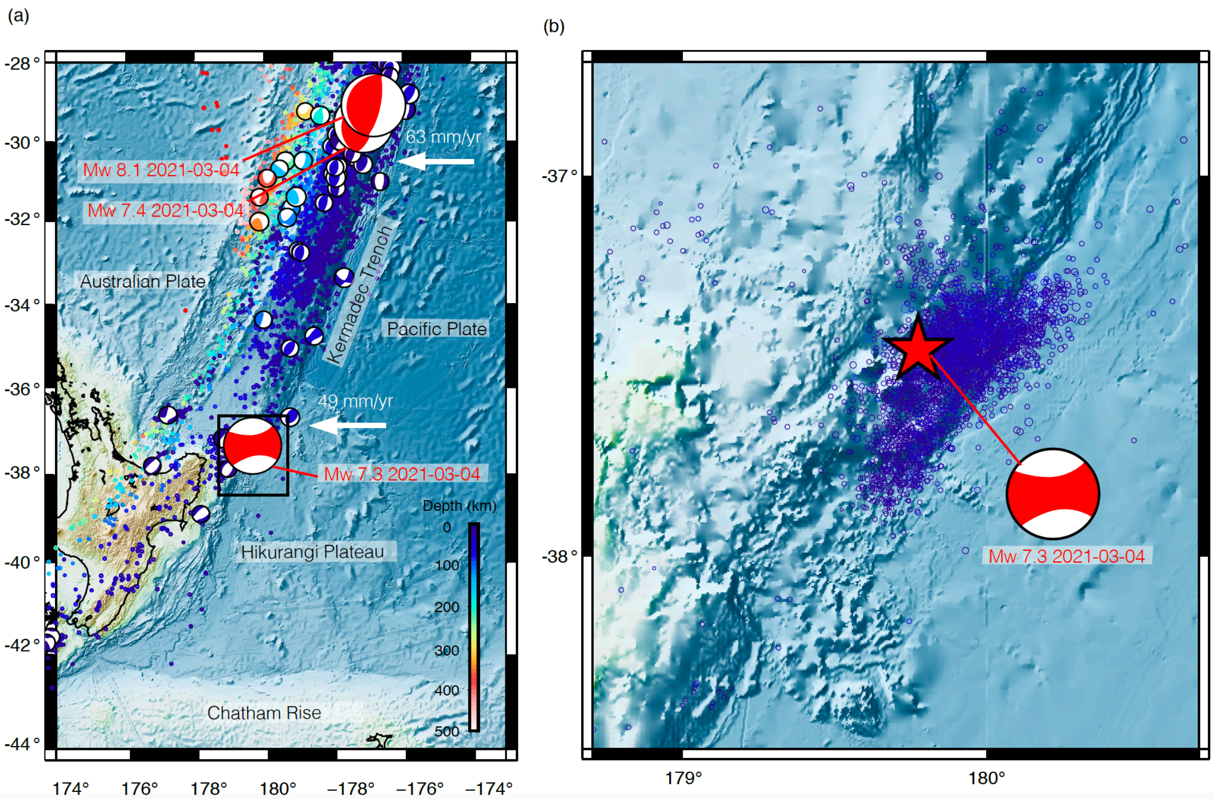


**Figure 1** Tectonic background of the Kermadec subduction zone and the seismicity near the Mw 7.3 earthquake. (**a**) The small circles are the EHB catalog (Engdahl et al., 1998) of M 4.5+ earthquakes from 1/15/1964 to 12/13/2017, color coded by depth. The beachballs are the CMT solution of M 6.5+ events (GCMT, Dziewonski et al., 1981; Ekström et al., 2012) from 1/1/1979 to 2/1/2021, color-coded by depth. The large red beachballs in (a) and (b) shows the CMT solutions (GCMT) of the 2017 earthquake sequence. The white arrow shows the slip rate of the Pacific plate relative to the Australian plate. The white arrows show the directions of Pacific-Australia plate convergence (de Mets et al., 1990). (**b**) The aftershock of M 2.5+ from 3/4/2021 to 5/13/2021 from the Geonet catalogue. The range of the map is shown by the black box in Figure 1(a). The star shows the epicenter of the Mw 7.3 earthquake.

There have been several Mw 6.5+ historical normal-faulting earthquakes but few large megathrust earthquakes around the source region of the 2021 Mw 7.3 earthquake. The only two recorded large interplate thrust earthquakes along the Hikurangi subduction zone are the 1947 Mw 7.1 Poverty Bay earthquake and the 1947 Mw 6.9-7.1 Tokomaru Bay earthquakes. Both of them are tsunamigenic with long source duration (~ 40 s) and slow rupture speeds (~1 km/s). They produced disproportionately large tsunamis for their magnitudes (Doser & Webb, 2003). The lack of large megathrust events in this region can be explained by the small interseismic plate coupling coefficient of ~ 0.6 at seismogenic depth from 0 to 10 km inferred from GPS studies (Wallace and Beavan, 2004; Wallace and Beavan, 2010). The plate convergence seems to be accommodated by repeating aseismic slow slip events, often found at the depth of 6 to 15 km, which marks the transition from the interseismic coupling and the deeper stable slipping portion of the plate interface (Wallace and Beavan, 2010). The most recently reported slow slip episodes, detected both before and after the 2016 Mw 7.0 earthquake, partially overlapped with the source area of the 2021 Mw 7.3 earthquake.

The Mw 7.3 earthquake is unusual in several aspects. The rupture lasted ~ 50 s according to the USGS earthquake W-phase inversion (Duputel et al., 2012), significantly longer than ~ 25 s for typical earthquakes of similar magnitudes (Ye et al., 2016). The focal mechanism is predominantly oblique-reverse, striking in the east-west direction where the historical M 6+ earthquakes are mostly normal-faulting events. The W-phase solution also suggests a 33% non-double couple component, which indicates that the earthquake ruptured multiple faults of different orientations. Okuwaki et al. (2021) conducted a finite fault inversion and a multiple point source inversion and concluded that this earthquake is composed of an initial subevent on an unexpected, deep trench-parallel compressional fault (50 to 100 km) and a second subevent on a shallow trench-normal extensional fault (0 to 30 km). The aftershocks span a large depth range from 0 km to 100 km (Fig. 2c). We find the aftershocks extend to ~ 30 km below the bottom of the slab according to the tomography and the background seismicity relocation result of Eberhart-Phillips & Bannister (2015) (Fig. 3e). Intraplate earthquakes at these depths are rare because brittle frictional failure is prohibited by high pressure and temperature. The mechanisms for such intermediate-depth earthquakes (70-250 km deep) are under debate. The leading hypotheses are (1) Fluid-aided embrittlement or weakening (Halpaap et al., 2019). (2) Rapid strain in fine-grained shear zones results in thermal runaway and highly localized zones of viscous failure (Kelemen & Hirth, 2007). The ruptures on distinctive fault planes are possibly related to the thick subducting buoyant oceanic plateau with widespread seamounts at East Cape. These seamounts are thought to produce complex fracture networks and favor small earthquakes or aseismic slip due to the presence of fluid-rich sediments and granular bands. The large earthquakes such as the Mw 7.3 event occur only when multiple small fractures coalesce, linked by static or dynamic triggering (Wang and Bilek (2011)).

Our aim is to resolve the details of the co-seismic rupture process of the Mw 7.3 earthquake and to understand the cause of its source complexity. The rest of the article is organized as follows. In section 2 we describe the method and results of multi-array 3D back projection imagery of the mainshock, which shows rupture on multiple distinctive faults. In section 3, we investigate the static and dynamic stress transfer between the two subevents. In section 4, we discuss the physical mechanisms of the deep ruptures and the triggering effects connecting the earthquake sequence.

## 2 Multi-Array 3D Back-Projection

Taking advantage of the development of dense regional seismic arrays, back-projection (BP) has become one of the most essential techniques to resolve rupture processes of large earthquakes (e.g. rupture lengths, directions, speeds and segmentation). Here we apply the Multi-taper 3D MUSIC Back-projection to resolve the spatial-temporal rupture process of the Mw 7.3 earthquake (Meng et al., 2011; Meng et al., 2015; Chen et al., 2018). We performed the 3D MUSIC BP separately on the P-wave seismograms of four broadband seismic arrays, composed of 211 stations along the western coast of continental US (US) (24 to 94°), 87 stations in South America (SA) (60 to 90°), 133 stations in Australia (AU) (30 to 60°) and 254 stations in China (CN) (82 to 89°) (Fig. S1), respectively. We check the BPs of a Mw 6.3 aftershock and the Mw 7.3 earthquake using the initial 10 s waveforms of individual arrays. The Mw 6.3 earthquake and the initial rupture of the Mw 7.3 earthquake can be regarded as a point source. Inspecting their BP images helps to understand the degree of smearing and aliasing effects. Fig. S2 and Fig. S3 show that individual arrays have limited spatial resolution, especially for depth. Fig. S2 and Fig. S3 show that the SA array alone has a good depth resolution longitudinally with a strong trade-off between along depth and latitude. The AU array alone has a good resolution latitudinally with a strong trade-off between depth and longitude. The combination of the SA and AU arrays should therefore achieve good vertical resolution. Similarly, the US array shows low resolution along the ray path (in the NE-SW direction). The CN array alone also smears in the NS-SE direction which is roughly perpendicular to the smearing of the US array. The combination of the CN and US arrays should therefore achieve good lateral resolution. Here, we combine BPs from individual arrays, which improves both depth and horizontal resolution (Fig. S2 and Fig. S3). Compared with single-array BPs, multi-array BPs enable higher spatiotemporal resolution and reduce false alarms in earthquake detection and location problems (Fan et al., 2018). The multi-array approach was also applied to improve stability and resolution of the BPs at local distances, where BPs of individual arrays may suffer large uncertainties due to crustal heterogeneities and simultaneous arrivals of multiple phases (Xie & Meng, 2020; Xie et al., 2021).

We first backproject the waveforms of individual arrays to a 3D source region surrounding the hypocenter. The imagery domain is 1 degree by 1 degree large, with the depth ranging from 0 to 140 km. The domain is divided into 100*100*140 grids with intervals of 0.01 degree in the horizontal directions and 1 km in the vertical direction. We choose the highest frequency band (0.5 to 2 Hz) with adequate waveform coherence at all arrays. (We require the average interstation correlation coefficients larger than 0.85 in the first 10 s of the P wave). We use the 1-D velocity model (e.g., IASP91) to estimate travel times and determine the relative location of the subsequent rupture with respect to the hypocenter. For each array, we aligned waveforms individually with a 6-second window centered on the P arrival using multi-channel cross-correlation to correct the travel time. This correction accounts for the travel-time anomalies due to heterogeneous earth structure, first introduced by Ishii et al. [2007]. The waveforms are back-projected to the source region in 10-seconds-long sliding windows with an increment of 1 second. We adopt the hypocenter relocated by Ryo Okuwaki et al. (2021) (-37.466N, 179.774E, 72 km). After we obtain the 3D back-projection images of the 4 arrays, we combine them by multiplying their MUSIC pseudo-spectrum at each grid in the source region. We choose to take the product of the BP images of each array to enhance the resolution. Note that to obtain the power of the combined BP (the black curve in Figure 2(b)), we take the sum of the normalized beamforming power of each array because it is more representative of the energy of the seismic radiation. We normalize the BP results of each array by their maximum amplitude during the main shock so that the four arrays are equally weighted. We choose equal weighting because the spatial resolutions of these arrays are complementary to each other, which provides independent constraint on the source location.

Figure 2 shows the result of the combined teleseismic 3D BP using 4 arrays. Fig. 2a and 2c show the 3D locations of the high-frequency (HF) radiators, which are defined as the peak locations of BP images and could be viewed as the centroid locations of the rupture front at each time frame. In the cases when there are two simultaneous strong peaks, we pick the secondary radiators from the BP image automatically using two requirements: (1) It is a local maximum (The BP amplitude is greater than all its neighboring grid points in x, y, and z direction (26 points in total)). (2) The secondary radiators need to be at least 20 km away from the primary one to avoid aliasing near the primary peak. The 3D locations of the radiators are in the supplemental material file 'S1.xlsx'. Fig. 2c shows that the rupture mainly propagates upward, from a depth of 72 km to the surface but propagates horizontally by only ~ 20 km to the northeast. Fig. 2d shows that in the first 20 s, the rupture propagates from depth D = 72 km to 50 km with a velocity of ~ 1 km/s. At T= 22 s, the main rupture abruptly split into two separated groups of radiators at D ~ 20 km and D ~ 80 km, possibly corresponding to simultaneous upward and downward propagating fronts, respectively. To understand the reliability of the combined BP, we inspect the results using just three of the four available arrays. Fig. S4 shows the BPs using different combinations of three arrays are consistent with the result using all four arrays, with the two groups of HF radiators in similar locations. The BP-imaged bilateral propagation is grossly consistent in location with the rupture episode E1 to E4 in Okuwaki et al. (2021). The abrupt splitting of the main rupture fronts might be caused by the resolution limit of BP (Xie et al., 2021). It is likely that the bilateral fronts exist before T = 22 s, but only their averaged/predominant location is imaged because their spatial separation did not yet meet the minimum resolvable length of the BP. In such a case, the rupture speed of 1 km/s of the apparent unilateral front should be slower than the actual rupture speed on the upward-propagating front. If we assume continuous bilateral propagation from the rupture initiation, the average rupture speed from 0 to 24 s to reach the segment at D ~ 20 km is ~ 2 km/s (Fig. 2d). Another possibility to explain the abrupt separations is that the rupture at D ~ 20 km is triggered on a separated fault. Given the upward propagation (~ 2 km/s) is slower than the P wave (~ 7 km/s) and S wave speeds (~ 4.3 km/s) at a depth of 40 km in this region (Eberhart-Philips et al., 2015), it is possible that either the P or S wave radiated from certain energetic episode of the early rupture triggered the fault segment at D = 20 km.

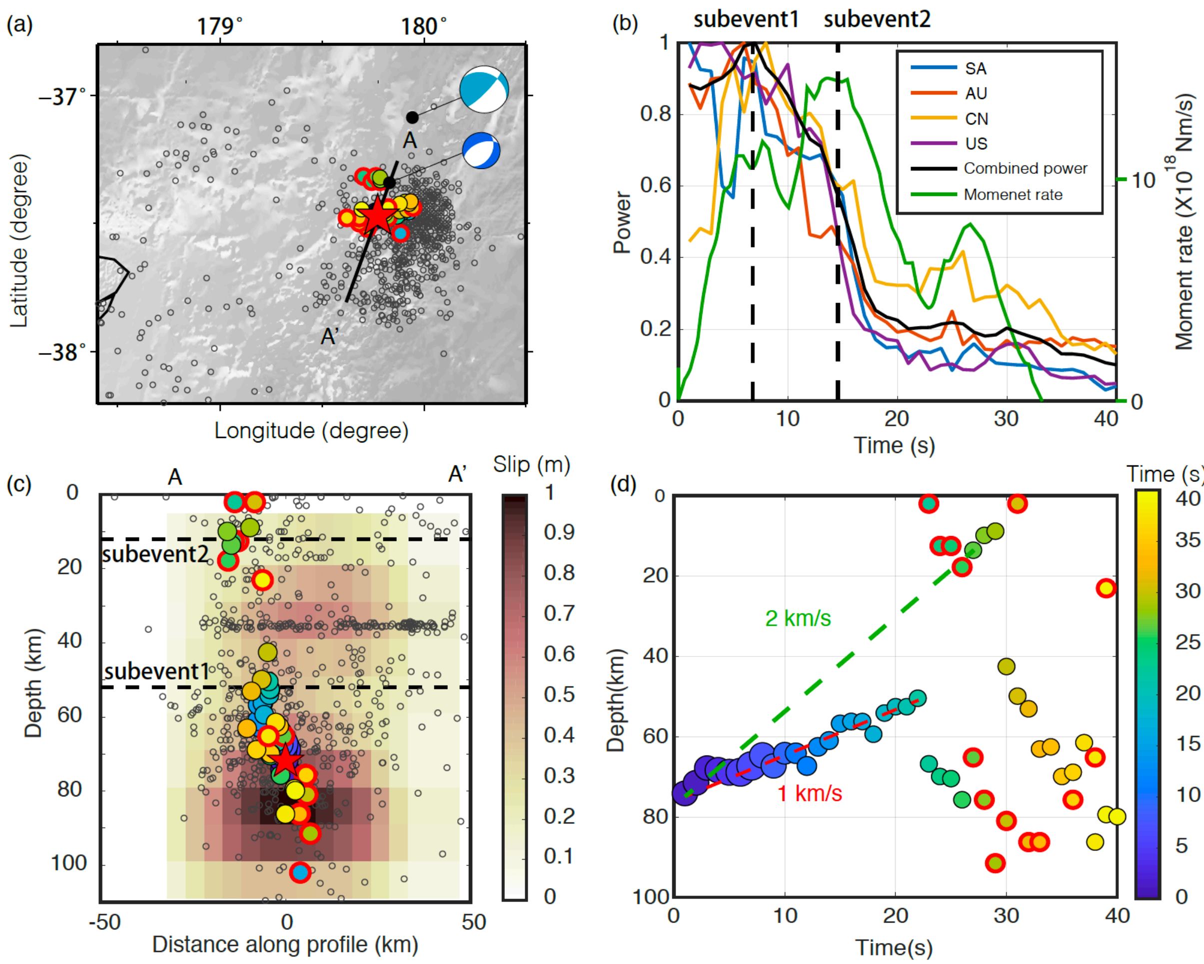


**Figure 2** Back-projection results of the Mw 7.3 earthquake after combining the images of 4 teleseismic arrays. (**a**) and (**c**) are the mapview and vertical cross-sections of the back-projection

results, respectively. The filled circles are the seismic radiators color-coded by time. The filled circles with red edges in (a), (c) and (d) are the second strongest peaks of BP images. The second strongest peaks are plotted only when their amplitude exceeds 50% of the strongest peak at a time step. The red star and small grey circles are the relocated mainshock and aftershocks by Okuwaki et al. (2021). The beach balls are multiple point source inversion results by Okuwaki et al. (2021) color coded by time. (**b**) The BP power at each time step. The moment rate of the slip model and the centroid time of the two subevents (dashed lines) are from Okuwaki et al. (2021). The combined power is the normalized sum of the normalized power of each array. (**d**) The relation between time and the depth of radiators. The red and the green dashed lines are the average rupture speed of the deep and shallow rupture fronts.

## 3 Static and dynamic stress transfer

To understand the triggering effect between the two subevents, we calculate the static Coulomb stress change on the assumed fault for Subevent 2 due to Subevent 1 using the software coulomb 3.3 (Lin and Stein, 2004) assuming a frictional coefficient of 0.4. We build simplified slip models based on the subevent inversion results. We get the depths, moments and fault orientations from subevent inversion results. Then we use the moment-dimension scaling relation (Wells and Coppersmith, 1994) to determine the fault length, width and slip assuming that the rigidity of the rock is 30 GPa (Table S1). The details of Coulomb stress calculation are in the supplemental material file 'S2.xlsx to S9.xlsx'. The results (Fig. 3 and Fig. S3) show that the maximum coulomb stress change is larger than 1 bar. There are no direct constraints to distinguish the two candidate fault planes of the two subevents. But we found that if Nodal Plane 1 is used for subevent 1, subevent 2 is in a positive coulomb stress region (Fig. 3 (a) (b) and Fig. S5 (a) (d)) with a magnitude of 0.06 bar on Nodal Plane 1 of Subevent 2 and 0.21 bar on Nodal Plane 2 of Subevent 2, respectively. If we use Nodal Plane 2 for Subevent 1, Subevent 2 is in a negative coulomb stress region (Fig. S5 (b) (e) (c) (f)). This indicates that for Subevent 1, Nodal Plane 1 is more likely to be the actual fault plane.

We also consider the dynamic stress triggering by examining the synthetic seismograms received at the centroid location of Subevent 2 generated from Subevent 1. The seismogram is computed with Qseis, a waveform simulator based on an orthonormal propagator algorithm assuming a layered viscoelastic half-space model (Wang, 1999). The results (Fig. 3(c)) show that the amplitude of the transverse component is the largest, with two pronounced arrivals at 13 s and 20 s, corresponding to S wave (4 km/s) and a reflected phase (2.4 km/s). We estimate the peak dynamic stress using the following equations (Jaeger & Cook, 1979):

$$\sigma = Gu/v_s,$$

where u is the peak velocity, which is estimated to be 0.2 m/s according to Fig. 3(c). $v_s$ is the phase velocity, which is ~ 3.34 km/s for S waves at a depth of 10 km according to a 1D velocity model (Kaneko et al., 2019). Given that the density $\rho$ is 2854 kg/m^3, the rigidity G is about 31.8 GPa ( $G = v_s{}^2 \cdot \rho$). The estimated peak stress $\sigma$ is approximately 19.1 bar, significantly larger than 0.1 bar, which is commonly considered the threshold of dynamic triggering (Brodsky & Prejean, 2005).

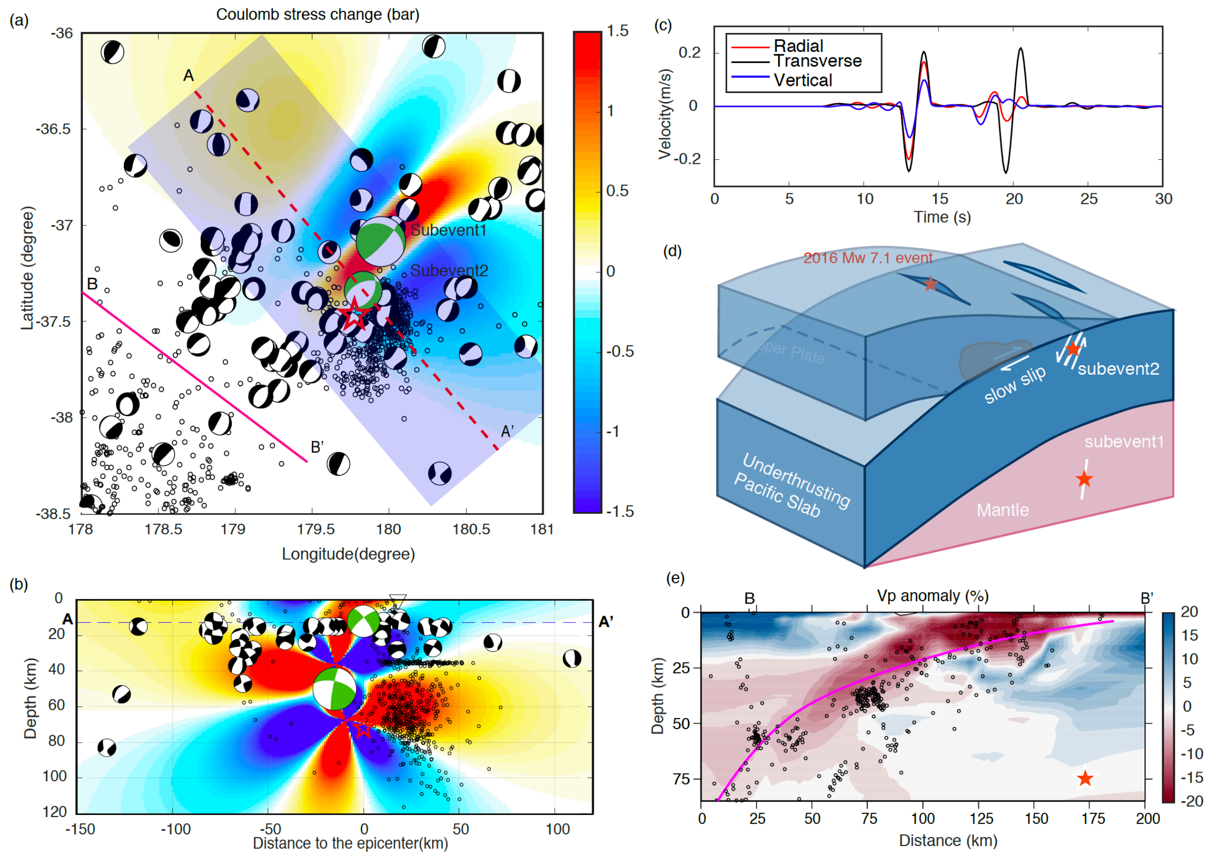


**Figure 3** Static and dynamic stress triggering and the schematic diagrams for the deep and shallow ruptures. (**a**) The horizontal cross-section (at depth of 12 km) of Coulomb stress change projected to the fault orientation corresponding to Subevent 2 (Nodal Plane 1, dip = 42°, rake=-120°, strike=29°) caused by Subevent 1 (Nodal Plane 1, dip=80°, rake=59°, strike=43°) based on the subevent inversion results of Okuwaki et al. (2021); The focal mechanisms and the locations of the two subevents are shown as the green beach balls in (a) and (b). The black beach balls show the focal mechanisms of the background seismicity from 1976/1/1 to 2021/1/1 (GCMT). The small black circles in (a) and (b) are the relocated aftershocks by Okuwaki et al. (2021) (**b**) The vertical cross-section of the coulomb stress changes along AA' (shown in Fig. 3a). The results for the other 3 combinations of candidate fault planes are shown in Fig. S3; The aftershocks and focal mechanism of background seismicity within 50 km from AA' (the shaded region in (a)) are projected onto the cross section. (**c**) Synthetic velocity seismograms at the centroid location of Subevent 2 simulated using the source parameters of Subevent 1; (**d**) The schematic diagrams showing the faults of the two subevents; (**e**) The vertical cross-section of the P wave velocity tomography along BB' (shown in Fig. 3a) and the background seismicity (modified from Fig. 5a in Eberhart-Phillips & Bannister, 2015)). The red star is the projected hypocenter of the Mw 7.3 earthquake along the direction parallel to the strike of the trench.

## 4 Summary and discussion

We combine the BPs of 4 teleseismic arrays to resolve the details of the rupture on multiple faults during the Mw 7.3 earthquake, which reveals that the earthquake is mainly composed of two episodes of rupture, with a deep rupture from D ~70 km to 50 km from 0 to 20 s, and a triggered rupture at D ~ 20 km from 20 to 40 s. The rupture regions and the bilateral pattern in the vertical direction are consistent with the finite fault slip model and the subevent inversion results of Okuwaki et al. (2021). We then evaluate the possibility that the shallow normal faulting event is triggered by the deep subevent with the effect of static and dynamic stress transfer separately.

### 4.1 Physical mechanisms of the deep rupture

The hypocenter relocated by Okuwaki et al. (2021) is at 72 km, which is below the lower plane of the double seismic zone and is in the slab mantle in this region (Fig. 3e). There is also a swarm of aftershocks from 50 to 80 km, most of which are in the regions with positive coulomb stress change (Fig. 3(b)). Earthquakes at these depths are rare because the subducting mantle is ductile (Duba, 1990). One possible mechanism of the initial deep rupture is that the failure is viscous due to heat produced by rapid strain in fine-grained shear zones, which was proposed by Kelemen & Hirth, (2007) and is used to explain the 2012 off-Sumatra earthquake that rupture the whole oceanic lithosphere (McGuire and Beroza, 2012).

Tomography of velocity structure in this region provides another possible explanation: the deep rupture may be caused by brittle failure due to delamination of the lower crust. Delamination is the sinking of part of the continental crust in the mantle due to increased density. The subducting Hikurangi plateau has a thick crust (12 to 15 km) thus possibly behaves like a continental plate and allows delamination. The tomography cross-section along A-A' (Fig. 3d, modified from Fig. 5a in Eberhart-Phillips & Bannister, 2015) shows a high Vp anomaly (3%-10%) region above the hypocenter. This Vp anomaly region is in the lower crust and uppermost mantle (150 to 200 km in horizontal direction, and 25 to 70 km in depth in Fig. 3(e)), which correlates with the location of the first sub-event. This low Vp anomaly indicates a delaminating lower crust, which enables the brittle failure and can explain the deep faulting in the slab mantle (Fillerup et al., 2010).

Another possibility for faulting in the slab mantle is related to fluid-aided embrittlement or weakening (Halpaap et al., 2019). The increasing pore pressure reduces effective normal stress and allows for earthquake rupture in high pressure and temperature conditions. Fluids may penetrate through the normal faulting, which is enhanced by the downward pumping effect by slab bending (Ranero et al., 2003; Faccenda et al., 2009). In Mariana, significant velocity reduction below the southernmost Mariana trench is observed, which provides evidence for such penetration (Wan et al., 2018). The velocity reduction is resolved with an array of ocean bottom seismometers above the Mariana trench and an active source seismic experiment. In the future, a similar experiment in the East Cape region can be performed to investigate this hypothesis. The fluid may also be fed from the lower region (Halpaap et al., 2019). Halpaap et al. (2019) observe seismicity at the depth of 60 to 80 km (~ 40 km below the bottom of the slab) in the subduction zone in Sanriku, Japan and Northeastern New Zealand, which is proposed to be related to fluid flow.

The second subevent is in the vicinity of historical normal faulting events (Fig. 3(a) and (b)), which are related to the normal faults activated or caused by slab bending (Masson, 1991; Ranero et al., 2003). The near parallel directions of the tectonic fabric and the axis of the bending (Fig. 1) further enhances the frequent normal faulting earthquakes (Ranero et al., 2003).

### 4.2 The role of the triggering effects in the earthquake sequence

The rupture of the shallow faulting is probably triggered by the rupture of the deep faulting. The Coulomb stress change on the assumed fault due to the rupture of the first fault is positive and over 0.2 bar. The peak dynamic stress is about 19.1 bar when assuming an elastic model. With the existence of the overlying sedimentary layers which amplifies the dynamic stress (Wallace et al., 2017), the amplitude of dynamic stress could be two orders of magnitude larger than the static stress change. The dynamic stress calculation is based on a point source. If considering the upward propagation of the initial rupture, the rupture directivity will result in elevated dynamic stress in the shallow region. The back-projection results show that the rupture of the shallow event starts around 20 s, which is coincidentally consistent with the timing of the reflected wave at ~ 20 s shown in fig. 3(c). It is also possible that the S wave radiated by the first subevent at a later time (e.g. ~ 7 s) triggers the shallow rupture.

The triggering of the rupture on the shallow faults has important implications for the potential earthquake and tsunami hazard in analog tectonic environments. Kiser et al. (2011) observed several doublets of intermediate-depth earthquakes in which subsequent subevents are dynamically triggered by the initial rupture at a distinct depth. They found the magnitude of the doublet earthquakes are among the largest of all intermediate-depth earthquakes. Thus, in seismic hazard analysis, it is important to consider the triggering of shallower faults by a deeper event which would otherwise generate weaker ground shaking. Similarly, shallow outer rise faults could also be triggered by deeper subduction earthquakes and produce large tsunamis, as is the case of the 2009 M8.1 Samoa earthquake (Lay et al., 2010).

The rupture of the subsequent Mw 7.4 and Mw 8.1 earthquakes occurred ~ 4 and ~6 hours later after the Mw 7.3 event, which are probably due to a delayed dynamic triggering of the Mw 7.3 earthquake considering the fast decay of the static stress with distance. Possible triggering mechanisms with delay include frictional properties changes (Parsons et al., 2005), pore fluid redistribution (Brodsky, 2005), triggering by slow slip or earthquakes that are instantaneously triggered (Brodsky, 2006; Shelly et al., 2011). Due to a lack of observation, we can not find more evidence for these mechanisms.

The Mw 7.4 and Mw 8.1 earthquakes are 900 km to the north of the Mw 7.3 earthquake. The two earthquakes are close to the Kermadec Islands, a region with dense historical M 7+ megathrust earthquakes. In contrast, the Mw 7.3 earthquake fails to trigger a few aftershocks along the subduction zone between the Mw 7.3 and the other two earthquakes, a 900-km-long section along the subduction zone. The low seismicity rate and the lack of large megathrust earthquakes from 38 °S to 34 °S indicates that this region may be a weakly coupled zone which accommodates shear deformation through ductile or aseismic slip. Its coupling condition may be similar to that of the eastern North Island based on GPS studies (Wallace and Beavan, 2010; Wang and Bilek, 2011). However, we take a cautionary note that the ~ 100 yrs recording history of larger earthquakes is not long enough to exclude the possibility that this region is well locked in an interseismic period.

**Acknowledgments**

This work is supported by the NSF CAREER grant EAR-1848486 and the Leon and Joanne V.C. Knopoff Fund. We thank Ryo Okuwaki, Stephen P. Hicks, Qibin Shi and Shenji Wei for valuable discussions about the tectonics and their discoveries of the 2021 Mw 7.3 East Cape earthquake. We thank Donna Eberhart-Phillips and Stephen Bannister for their help with downloading the velocity model.

**Open Research**

For the teleseismic back-projection, we downloaded the seismic waveforms of the US, SA and AU Array from IRIS Data Services (https://ds.iris.edu/wilber3/find_event).

The facilities of IRIS Data Services, and specifically the IRIS Data Management Center, were used for access to waveforms, related metadata, and/or derived products used in this study. IRIS Data Services are funded through the Seismological Facilities for the Advancement of Geoscience (SAGE) Award of the National Science Foundation under Cooperative Support Agreement EAR-1851048. We used the following networks and acknowledge them as follows:

AE:Arizona Geological Survey. (2007). Arizona Broadband Seismic Network [Data set]. International Federation of Digital Seismograph Networks. https://doi.org/10.7914/SN/AE

AU: Australian National Seismograph Network. H., G., & Geoscience Australia. (2021). Australian National Seismograph Network Data Collection (Version 2.0, September 2018) [Data set]. Commonwealth of Australia (Geoscience Australia). https://doi.org/10.26186/144675

AZ:UC San Diego. (1982). ANZA Regional Network [Data set]. International Federation of Digital Seismograph Networks. https://doi.org/10.7914/SN/AZ

BK: Northern California Earthquake Data Center. (2014). Berkeley Digital Seismic Network (BDSN) [Data set]. Northern California Earthquake Data Center. https://doi.org/10.7932/BDSN

C: Chilean National Seismic Network. (No DOI is registered for this network).

C1: Universidad de Chile. (2012). Red Sismologica Nacional [Data set]. International Federation of Digital Seismograph Networks. https://doi.org/10.7914/SN/C1

CI: California Institute of Technology and United States Geological Survey Pasadena. (1926). Southern California Seismic Network [Data set]. International Federation of Digital Seismograph Networks. https://doi.org/10.7914/SN/CI

CX:GFZ German Research Centre For Geosciences, & Institut Des Sciences De L'Univers-Centre National De La Recherche CNRS-INSU. (2006). IPOC Seismic Network. Integrated Plate boundary Observatory Chile - IPOC. https://doi.org/10.14470/PK615318

G: Institut de physique du globe de Paris (IPGP), & École et Observatoire des Sciences de la Terre de Strasbourg (EOST). (1982). GEOSCOPE, French Global Network of broad band seismic stations. Institut de physique du globe de Paris (IPGP), Université de Paris. https://doi.org/10.18715/GEOSCOPE.G

GE: GEOFON Data Centre. (1993). GEOFON Seismic Network. Deutsches GeoForschungsZentrum GFZ. https://doi.org/10.14470/TR560404

GT: Albuquerque Seismological Laboratory (ASL)/USGS. (1993). Global Telemetered Seismograph Network (USAF/USGS) [Data set]. International Federation of Digital Seismograph Networks. https://doi.org/10.7914/SN/GT

II: Scripps Institution of Oceanography. (1986). Global Seismograph Network - IRIS/IDA [Data set]. International Federation of Digital Seismograph Networks. https://doi.org/10.7914/SN/II

IU: Albuquerque Seismological Laboratory (ASL)/USGS. (1988). Global Seismograph Network - IRIS/USGS [Data set]. International Federation of Digital Seismograph Networks. https://doi.org/10.7914/SN/IU

MI: USGS Alaska Anchorage. (2000). USGS Northern Mariana Islands Network [Data set]. International Federation of Digital Seismograph Networks. https://doi.org/10.7914/SN/MI

MX: Red Sísmica Mexicana. (n.d.). https://doi.org/10.21766/SSNMX/SN/MX

MY: Malaysian National Seismic Network (No DOI is registered for this network).

NR: Utrecht University (UU Netherlands). (1983). NARS [Data set]. International Federation of Digital Seismograph Networks. https://doi.org/10.7914/SN/NR

PB: Plate Boundary Observatory Borehole Seismic Network (No DOI is registered for this network.)
PN: PEPP-Indiana(No DOI is registered for this network.)
PT: Pacific Tsunami Warning Center. (1965). Pacific Tsunami Warning Seismic System [Data set]. International Federation of Digital Seismograph Networks. https://doi.org/10.7914/SN/PT
PY: UC San Diego. (2014). Piñon Flats Observatory Array [Data set]. International Federation of Digital Seismograph Networks. https://doi.org/10.7914/SN/PY
RB: Red Sísmica de Banda Ancha(No DOI is registered for this network.)
S1: Australian National University (ANU, Australia). (2011). Australian Seismometers in Schools [Data set]. International Federation of Digital Seismograph Networks. https://doi.org/10.7914/SN/S1
SB: UC Santa Barbara. (1989). UC Santa Barbara Engineering Seismology Network [Data set]. International Federation of Digital Seismograph Networks. https://doi.org/10.7914/SN/SB
YB: John Louie. (2017). Yosemite Valley Deep Refraction Microtremor [Data set]. International Federation of Digital Seismograph Networks. https://doi.org/10.7914/SN/YB_2017
YN: Frank Vernon, & Yehuda BenZion. (2010). San Jacinto Fault Zone Experiment [Data set]. International Federation of Digital Seismograph Networks. https://doi.org/10.7914/SN/YN_2010

## Data Availability Statement

The 3D locations of the radiators (S1.xlsx) and the details of Coulomb stress (S2.xlsx to S9.xlsx) calculation are uploaded to Zenodo with doi:10.5281/zenodo.6987914.

## References


Brodsky, E. E., & Prejean, S. G. (2005). New constraints on mechanisms of remotely triggered seismicity at Long Valley Caldera. Journal of Geophysical Research: Solid Earth, 110(B4).

Brodsky, E. E. (2006). Long-range triggered earthquakes that continue after the wave train passes. Geophysical Research Letters, 33(15).

Chen, Y., Meng, L., Zhang, A., & Wen, L. (2018). Source complexity of the 2015 Mw 7.9 Bonin earthquake. Geochemistry, Geophysics, Geosystems, 19(7), 2109-2120.

Collot, J. Y., & Davy, B. (1998). Forearc structures and tectonic regimes at the oblique subduction zone between the Hikurangi Plateau and the southern Kermadec margin. Journal of Geophysical Research: Solid Earth, 103(B1), 623-650.

de Mets, C., Gordon, R. G., Argus, D. F., & Stein, S. (1990). Current plate motions. Geophysical journal international, 101(2), 425-478.

Doser, D. I., & Webb, T. H. (2003). Source parameters of large historical (1917–1961) earthquakes, North Island, New Zealand. Geophysical journal international, 152(3), 795-832.

Duba, A. G., Durham, W. B., Heard, H. C., Handin, J. W., & Wang, H. F. (Eds.). (1990). The brittle-ductile transition in rocks: The Heard Volume. American Geophysical Union.

Duputel, Z., Rivera, L., Kanamori, H., & Hayes, G. (2012). W phase source inversion for moderate to large earthquakes (1990–2010). Geophysical Journal International, 189(2), 1125-1147.

Dziewonski, A. M., T.-A. Chou and J. H. Woodhouse, Determination of earthquake source parameters from waveform data for studies of global and regional seismicity, J. Geophys. Res., 86, 2825-2852, 1981. doi:10.1029/JB086iB04p02825

Eberhart-Phillips, and Donna, Bannister, Stephen. "3-D imaging of the northern Hikurangi subduction zone, New Zealand: variations in subducted sediment, slab fluids and slow slip." Geophysical Journal International 201.2 (2015): 838-855.

Engdahl, E.R., R. van der Hilst, and R. Buland (1998). Global teleseismic earthquake relocation with improved travel times and procedures for depth determination, Bull. Seism. Soc. Am. 88, 3, 722-743.

Faccenda, M., Gerya, T. V., & Burlini, L. (2009). Deep slab hydration induced by bending-related variations in tectonic pressure. Nature Geoscience, 2(11), 790-793.

Fan, W., de Groot-Hedlin, C. D., Hedlin, M. A., & Ma, Z. (2018). Using surface waves recorded by a large mesh of three-element arrays to detect and locate disparate seismic sources. Geophysical Journal International, 215(2), 942-958.

Fillerup, M. A., Knapp, J. H., Knapp, C. C., & Raileanu, V. (2010). Mantle earthquakes in the absence of subduction? Continental delamination in the Romanian Carpathians. Lithosphere, 2(5), 333-340.

Halpaap, F., Rondenay, S., Perrin, A., Goes, S., Ottemöller, L., Austrheim, H., ... & Eeken, T. (2019). Earthquakes track subduction fluids from slab source to mantle wedge sink. Science advances, 5(4), eaav7369.

Ishii, M., Shearer, P. M., Houston, H., & Vidale, J. E. (2007). Teleseismic P wave imaging of the 26 December 2004 Sumatra-Andaman and 28 March 2005 Sumatra earthquake ruptures using the Hi-net array. Journal of Geophysical Research: Solid Earth, 112(11), 1–16. https://doi.org/10.1029/2006JB004700

Jaeger, J. C., & Cook, N. G. W. (1979). Fundamentals of rock mechanics. Chapman and Hall, London, 593 pp.

Kaneko, Y., Ito, Y., Chow, B., Wallace, L. M., Tape, C., Grapenthin, R., ... & Hino, R. (2019). Ultra-long duration of seismic ground motion arising from a thick, low-velocity sedimentary wedge. Journal of Geophysical Research: Solid Earth, 124(10), 10347-10359.

Kelemen, P. B., & Hirth, G. (2007). A periodic shear-heating mechanism for intermediate-depth earthquakes in the mantle. Nature, 446(7137), 787-790.

Kennett, B. L. N., & Engdahl, E. R. (1991). Traveltimes for global earthquake location and phase identification. Geophysical Journal International, 105(2), 429-465.

Lay, T., Ammon, C. J., Kanamori, H., Rivera, L., Koper, K. D., & Hutko, A. R. (2010). The 2009 Samoa–Tonga great earthquake triggered doublet. Nature, 466(7309), 964-968.

Lin, J., & Stein, R. S. (2004). Stress triggering in thrust and subduction earthquakes and stress interaction between the southern San Andreas and nearby thrust and strike-slip faults. Journal of Geophysical Research: Solid Earth, 109(B2).

Masson, D. G. (1991). Fault patterns at outer trench walls. Marine Geophysical Researches, 13(3), 209-225.

McGuire, J. J., & Beroza, G. C. (2012). A rogue earthquake off Sumatra. Science, 336(6085), 1118-1119.

Meng, L., Inbal, A., & Ampuero, J. P. (2011). A window into the complexity of the dynamic rupture of the 2011 Mw 9 Tohoku-Oki earthquake. Geophysical Research Letters, 38(7).

Meng, L., Huang, H., Bürgmann, R., Ampuero, J. P., & Strader, A. (2015). Dual megathrust slip behaviors of the 2014 Iquique earthquake sequence. Earth and Planetary Science Letters, 411, 177-187.

Okuwaki, R., Hicks, S. P., Craig, T. J., Fan, W., Goes, S., Wright, T. J., & Yagi, Y. (2021). Illuminating a contorted slab with a complex intraslab rupture evolution during the 2021 Mw 7.3 East Cape, New Zealand earthquake. Geophysical Research Letters, e2021GL095117.

Parsons, T. (2005). A hypothesis for delayed dynamic earthquake triggering. Geophysical Research Letters, 32(4).

Ranero, C. R., Morgan, J. P., McIntosh, K., & Reichert, C. (2003). Bending-related faulting and mantle serpentinization at the Middle America trench. Nature, 425(6956), 367-373.

Shelly, D. R., Peng, Z., Hill, D. P., & Aiken, C. (2011). Triggered creep as a possible mechanism for delayed dynamic triggering of tremor and earthquakes. Nature Geoscience, 4(6), 384-388.

Wallace, L. M., Kaneko, Y., Hreinsdóttir, S., Hamling, I., Peng, Z., Bartlow, N., ... & Fry, B. (2017). Large-scale dynamic triggering of shallow slow slip enhanced by overlying sedimentary wedge. Nature Geoscience, 10(10), 765-770.

Wan, K., Lin, J., Xia, S., Sun, J., Xu, M., Yang, H., ... & Xu, H. (2019). Deep seismic structure across the southernmost Mariana Trench: Implications for arc rifting and plate hydration. Journal of Geophysical Research: Solid Earth, 124(5), 4710-4727.

Wells, D. L., & Coppersmith, K. J. (1994). New empirical relationships among magnitude, rupture length, rupture width, rupture area, and surface displacement. Bulletin of the seismological Society of America, 84(4), 974-1002.

Xie, Y., & Meng, L. (2020). A multi-array back-projection approach for tsunami warning. Geophysical Research Letters, 47(14), e2019GL085763.

Xie, Y., Bao, H., & Meng, L. (2021). Source Imaging With a Multi-Array Local Back-Projection and Its Application to the 2019 Mw 6.4 and Mw 7.1 Ridgecrest Earthquakes. Journal of Geophysical Research: Solid Earth, 126(10), e2020JB021396.

Ye, L., Lay, T., Kanamori, H., & Rivera, L. (2016). Rupture characteristics of major and great (Mw≥ 7.0) megathrust earthquakes from 1990 to 2015: 1. Source parameter scaling relationships. Journal of Geophysical Research: Solid Earth, 121(2), 826-844.

Wallace, L. M., Beavan, J., McCaffrey, R., & Darby, D. (2004). Subduction zone coupling and tectonic block rotations in the North Island, New Zealand. Journal of Geophysical Research: Solid Earth, 109(B12).

Wallace, L. M., & Beavan, J. (2010). Diverse slow slip behavior at the Hikurangi subduction margin, New Zealand. Journal of Geophysical Research: Solid Earth, 115(B12).

Wang, K., & Bilek, S. L. (2011). Do subducting seamounts generate or stop large earthquakes?. Geology, 39(9), 819-822.

Wang, R. (1999). A simple orthonormalization method for stable and efficient computation of Green's functions. Bulletin of the Seismological Society of America, 89(3), 733-741.